December 2020

A Stochastic Model for the Aerodynamics of Irregularly Shaped Gravel

Md Safwan Ahsanullah
Clemson University, safwanahsanullah@gmail.com

A STOCHASTIC MODEL FOR THE AERODYNAMICS OF IRREGULARLY SHAPED GRAVEL

A Thesis
Presented to
the Graduate School of
Clemson University

In Partial Fulfillment
of the Requirements for the Degree
Master of Science
Civil Engineering

---

by
Md Safwan Ahsanullah
December 2020

Accepted by:
Dr. Nigel B. Kaye, Committee Chair
Dr. Abdul A. Khan
Dr. William C. Bridges Jr.

ABSTRACT

The flight of compact debris has numerous uncertainties associated and can be highly stochastic in nature. Standard flight equations fail to take a lot of these aspects into account because of the assumption of the debris particle being spherical in shape. This study proposes a stochastic model in an attempt to resolve some key aspects of the said uncertainties originated due to the change in orientation of the debris particle during its flight, and as a result the alteration of the projected cross-sectional area, the lift and the drag coefficients. The model numerically solves the differential equations of motion for a large number of gravel pieces taken from five different size gradations. The amount by which the drag and lift coefficients (δC_D and δC_L), the orientation ($\delta\theta$) and the projected area ($\delta\alpha$) are varied at each time-step during the flight simulation of a single debris are the four parameters used to fit the model to the results obtained from gravel drop experiments. An optimization criterion (ε) has been introduced and the model has been optimized individually for each gradation and globally across gradations of different gravel sizes. Upon observing the spread of the landing locations and their radial distances obtained from the model under its optimized conditions, it has been found that while the variation of lift coefficient appears to have a minimal impact on the trajectory of the particle, the change in orientation, drag coefficient and projected area are important factors to be continuously perturbed to be able to correctly track the landing locations for a sufficient number of gravel pieces. The individual optimization technique has also proven to perform better than the global optimization, which is expected as the gravel gradations are geometrically dissimilar.

DEDICATION

To my parents, Ahsanullah and Fatema, and my siblings, Redwan and Salman. For their love towards me has been the only constant in this ever-changing universe!

ACKNOWLEDGMENTS

I would like to express my sincere gratitude to my research advisor, Dr. Nigel B. Kaye, for his continuous support and guidance throughout the pursuit of my graduate degree. It would not have been possible for me to get this work accomplished successfully without your skilled tutelage and mentorship.

I also want to acknowledge my graduate committee members Dr. Abdul A. Khan, for his kind assistance and cooperation, and Dr. William C. Bridges Jr., for his valuable insights and guidance through the process.

I am thankful to Megan Holmes for running the experiments and collecting all the experimental data. You have been a highly resourceful member of the team, and this has definitely been a great experience for me to have worked with you on this study.

I acknowledge the unconditional love and support of my family and friends, both here and back home. Your love and inspiration have been a great source of motivation for me and I am eternally in your debt.

This material is based upon work supported by the National Science Foundation under Grant No. 1760999. Any opinions, findings, and conclusions or recommendations expressed in the material are those of the author and do not necessarily reflect the views of the NSF.

TABLE OF CONTENTS

Table of Contents (Continued)

Page

LIST OF TABLES

LIST OF FIGURES

List of Figures (Continued)

Figure Page

CHAPTER ONE

INTRODUCTION

Role of Wind-borne Debris

Wind-borne debris and missiles in events of severe windstorms, hurricanes and, other strong wind events have been observed to cause significant damage to the built environment. After more than thirty years of research on hundreds of post-storm investigations, Minor (2005) [1] has concluded that the building envelope is crucial to satisfactory performance of buildings in windstorms and wind-driven debris is a decisive factor in determining the performance of the building envelope. Field investigations show how the entire structure of a building suffers from cascading failure following the first failure of the envelope. Leakage of the building envelope due to impact by fast-moving debris exposes the conditioned space within the building to the external unconditioned environment. This results in increased rain and debris infiltration, causing further damage to the contents within the interior of the building. This can also lead to internal pressurization and increased roof uplift, which can, in severe cases, cause roof lift-off. Smith & McDonald (1990) [2] stated in their report following Hurricane Hugo (Charleston, SC-1989) that, the damage to the inside of the building and the contents within due to water infiltration can cause greater financial loss than the damage to building structure itself. Thorough assessments of insurance records following strong wind events also show a dramatic increase in the total financial loss for damages that involve breaching of building envelope. Sparks et al. (1994) [3] related wind speed to the damage claims and concluded

that the size of claims is greater when the building envelope is compromised in the events of storms and hurricanes.

There has been extensive studies and literature for decades, corroborated by thorough post-hurricane investigations, on the role of wind-borne debris on built environment. Reports after notable wind events such as Hurricane Hugo (1989, Charleston SC), Hurricane Andrew (1992, South Florida), Hurricane Alicia (1983, Houston TX) show that the wind-borne debris had been a major contributor to the total economic loss [1]. Several studies following Hurricane Alicia have shown that blown-off roof gravel caused significant damage to the window glasses of high-rise buildings in Downtown Houston [4]. Behr and Minor (1994) [5] have also drawn similar conclusions after Hurricane Andrew, which caused an estimated total of US$ 26.5 billion in damage according to the report by United States National Hurricane Center [6]. In their report one year after Hurricane Hugo, Smith and McDonald (1990) [2] have presented that the blown-off gravel can cause severe injury and property damage, and in one case, aggregate has been recorded to have traveled more than 245 ft (75 m) from one building to another breaking nearly all of the outer panes of double-glazed windows and a number of inner panes as well. In an attempt to address the issue of damage from wind-borne debris, building design codes have gone through several modifications over time and the existing design guidelines have still proven to fall short at times with debris motion initiation occurring at wind speeds lower than the design wind speeds. There still exists a significant knowledge gap around the motion initiation mechanism and resulting flight. These criteria can be solved only with a deeper understanding of the forces acting on particles of random shapes.

Debris Classification

Debris has been classified in different ways based on their shape, size, weight and locations. However, the most commonly used scheme of debris classification while modeling debris flight, proposed by Wills et al. (2002) [7], classifies the debris in three

(a)

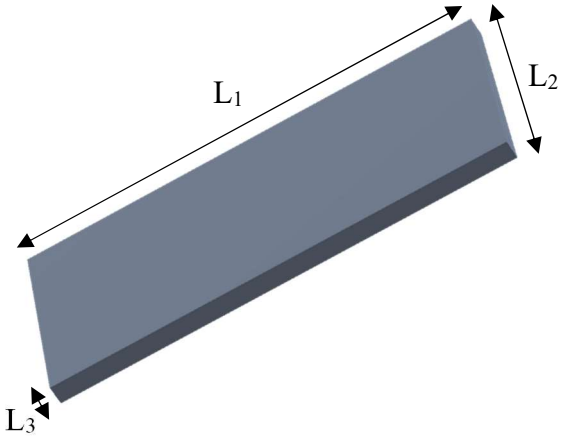

(b)

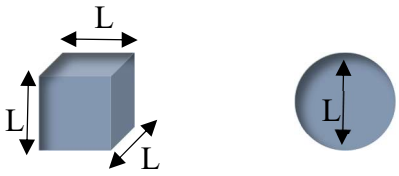

(c)

Figure 1: Classification of Debris with dimensions (a) Rod-like Debris ($L_1 >> L_2$), (b) Plate-like Debris ($L_1, L_2 >> L_3$), (c) Compact Debris ($L_1 \approx L_2 \approx L_3 \approx L$)

types (shown in Figure 1) based on their geometric shape : rod-like (linear debris), plate-like (planar debris) and compact debris (three dimensional debris).

- Rod-like debris has one dimension significantly larger than the other two,
- Plate-like debris has two dimensions significantly larger than the third one, and
- Compact debris has similar dimensions in all three directions.

Motivation

The standard compact debris flight equations assume that the debris can be treated as spherical (Baker 2007 [8], Holmes 2004 [9]) and that it does not rotate. The consequences of these assumptions are that

1. There are no aerodynamic moments acting on the debris
2. There are no lift forces acting on the debris,
3. The debris cross-sectional area is independent of orientation, and, therefore,
4. The only forces acting on the debris are the debris weight (vertically down) and aerodynamic drag acting in the direction of the apparent wind.

These assumptions lead to the derivation of the compact debris flight equations which, for a straight-line wind, are two dimensional. They can be written as a set of two coupled second order ordinary differential equations

$$\frac{d^2x}{dt^2} = \frac{du}{dt} = \frac{\rho C_D A}{2m}(U-u)\sqrt{(U-u)^2+w^2} \tag{1}$$

and

$$\frac{d^2z}{dt^2} = \frac{dw}{dt} = \frac{\rho C_D A}{2m}(-w)\sqrt{(U-u)^2+w^2} - g \tag{2}$$

In the above equations x is the horizontal coordinate in the direction of the wind flow, z is vertically upward, m is the mass of the debris, ρ is the fluid density, C_D is the drag coefficient (often assumed to be constant), g is acceleration due to gravity, U is the wind speed (taken to be uniform and horizontal), and u and w are the horizontal and vertical components of the debris particle velocity in the horizontal and vertical directions respectively. For a long enough flight distance these equations yield a solution in which the debris travels horizontally at the wind speed and vertically at its terminal velocity.

However, irregularly shaped compact debris does not travel in a two-dimensional plane. This can be observed by dropping small pieces of gravel into a tank of water and observing that they do not fall vertically. Observations from such experiments indicate that

1. The gravel pieces rotate during their fall
2. Their fall is not vertical or, in fact, even in a straight line,
3. The path varies from one piece to the next even for gravel pieces taken from the same gravel gradation.

When a piece of gravel is released from rest it will initially fall vertically because the only forces acting on it, are its weight down and the buoyancy force up (assumed negligible when falling through air, but significant when falling through water). At this point the apparent fluid velocity, that is, the fluid velocity relative to the gravel, will be vertically up. Therefore, any deviation of the flight path from vertical must be the result of a lift force (i.e. an aerodynamic force that acts normal to the direction of the apparent fluid velocity). Further, since the gravel is observed to rotate during flight, the cross-sectional

area of the gravel normal to the apparent fluid velocity will vary. These observations violate all four of the assumptions listed above.

To better understand the flight of irregularly shaped compact debris an experimental and modeling study was undertaken and is presented below. In chapter 2 the experimental methods are described including details of the data analysis and data processing. Experimental results are presented in chapter 3 including qualitative descriptions of the flight paths and detailed statistical analysis of the landing locations of the various gravel pieces dropped. These observations are used to develop a stochastic flight model for gravel pieces falling through a stagnant environment (chapter 4). The results are discussed in chapter 5, and conclusions are drawn in chapter 6.

CHAPTER TWO

EXPERIMENTAL METHOD

Experimental Setup

To gain insight on the motion of irregularly shaped gravel pieces moving through a fluid, a simple experimental setup is designed for this study. The setup consists of a clear-sided tank filled with water and gravel pieces of different sizes as representative of a typical compact debris (shown in Figure 2).

Figure 2: Some samples of the gravel pieces used in the experiment

The main objective of the experiment is to observe the spread of the landing locations of dropped gravel pieces. An earth-fixed, right-handed coordinate system is defined with its origin fixed at the center of the cross-section of the tank. The x and y-axes are on the horizontal plane as shown in Figure 3 while the z-axis points vertically upwards.

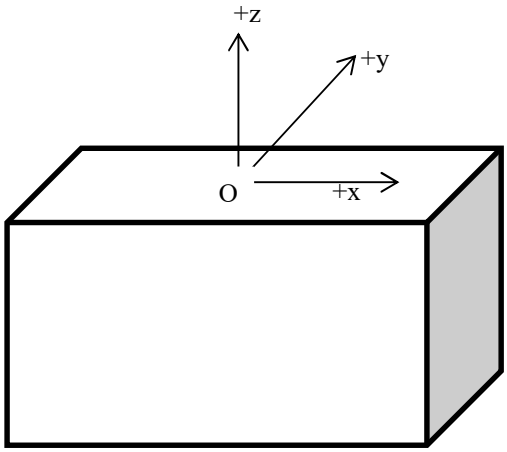

Figure 3: Schematic diagram of the water tank and the system of coordinates

Table 1 shows the dimensions of the tank used for the experiment:

Table 1: Dimension of the tank used in the experiments

Inside Dimensions of Tank	
Length	0.5906 m
Width	0.2921 m
Height	0.4001 m
Top of sand layer to water surface	0.3747 m

Experimental Procedure

To locate the center of the cross-section (the origin), fishing wire was stretched from corner to corner diagonally. Each piece of gravel was released from the center, directly below the point where the wires intersect each other. A thin uniform layer of sand was placed on the bottom of the tank to prevent gravel pieces from bouncing off the floor. For each gravel size, sets of 20 were dropped at a time for easier identification of the

landing locations and reduced chance of gravel pieces piling on top of each other or bouncing off one another. After each set, an aerial photo of the spread was taken from directly above the fish tank for further analyses. Figure 4 shows a sample of such photo:

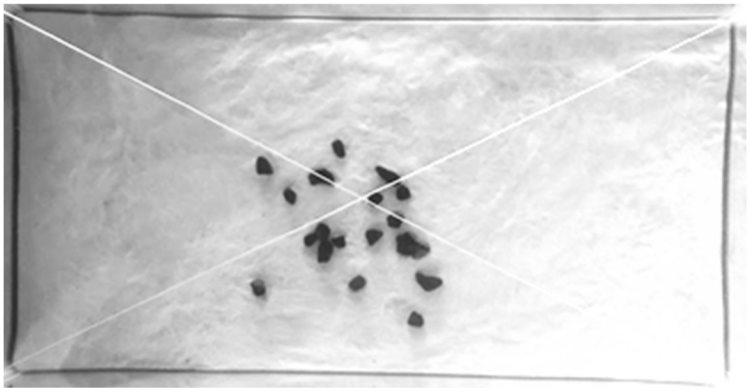

Figure 4: A sample aerial photo of landing locations of 20 dropped gravel pieces

From each aerial photo, the landing locations were digitized as a scatter plot with respect to a given 2D coordinate system. From the resulting x-y coordinates of the landing locations, the radial distance of each point can easily be extracted from the center of the tank base (directly below the release point).

Measurement Technique

To digitize the landing locations, ScanIt by *AmsterCHEM* [10] was used. This software takes an image file and allows the user to create a 2D coordinate system. Based on this defined coordinate system, each landing location is assigned a pair of x-y coordinates which can be exported to a spreadsheet. The radial distances of the landing locations from the center of the tank base is calculated using the exported data. Figure 5 below shows the user interface of the software.

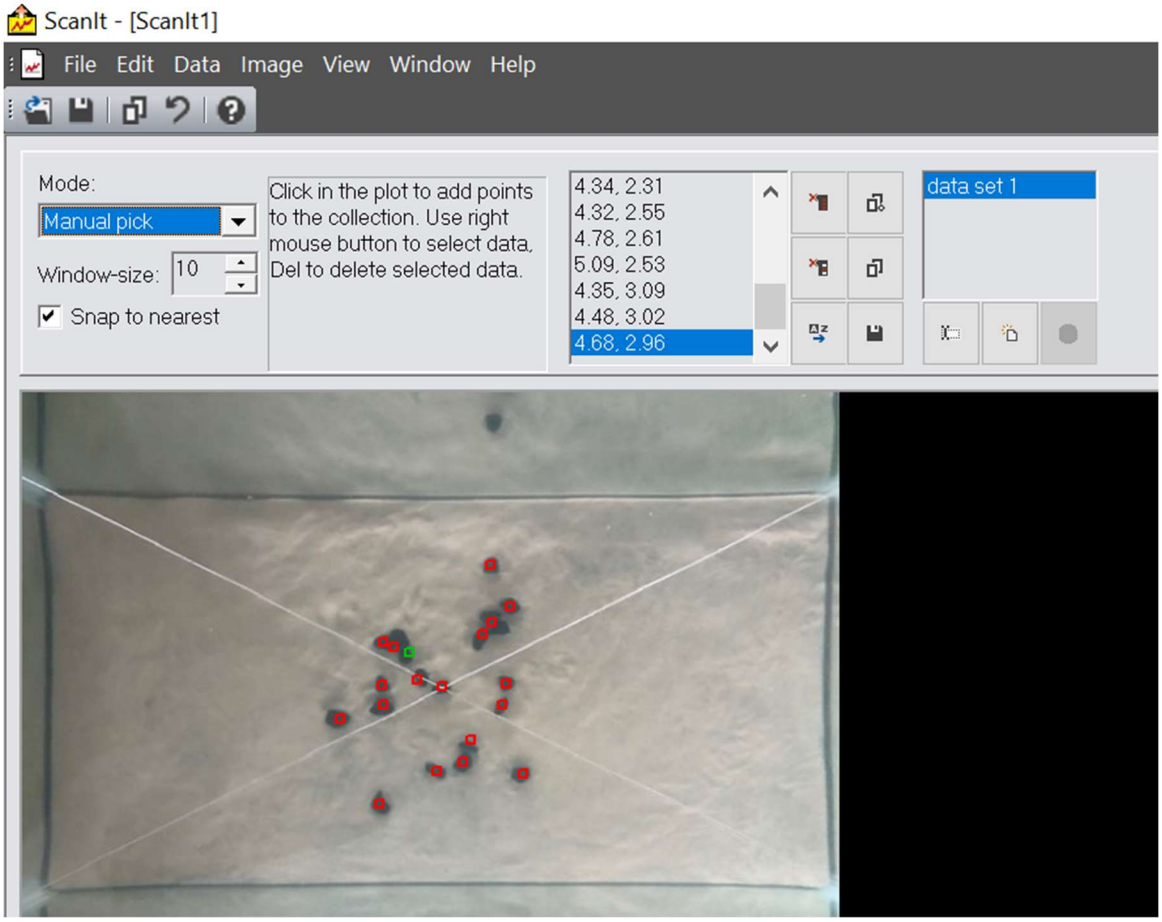

Figure 5: User interface of ScanIt showing extraction of coordinates for landing locations from a sample aerial photo

Statistical Description of Gravel Size and Shape

For the experiment in this study, five different sizes of gravel pieces have been used denoted as gradations A, B, C, D and E from largest to smallest size in order of their mean equivalent radii. For each of the five gravel sizes, a sample of 45 pieces was randomly selected, and lengths along the shortest dimension (L_1), the longest dimension (L_3) and in the direction perpendicular to L_1 and L_3 were measured (L_2). Figure 6 shows a representation of L_1, L_2 and L_3 measurements for a sample gravel piece:

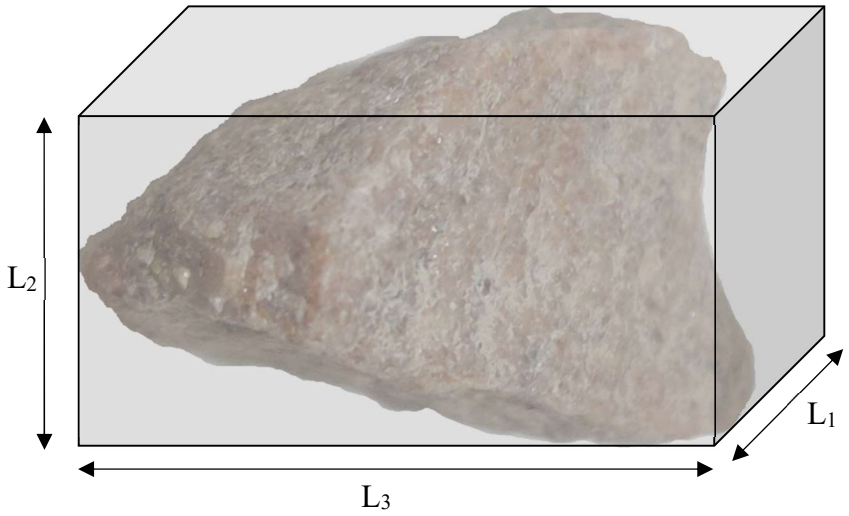

Figure 6: A gravel piece with bounding cuboid showing length measurements along the three directions (L_1, L_2 and L_3)

Both L_1 and L_2 were, then, normalized by the longest dimension (L_3) to assess the size variation across the gravel gradations. The mean volume of the gravel pieces for each sample is calculated by placing a number of these gravels in water inside a measuring cylinder and observing the volume of displaced water. From the mean volumes, mean equivalent radii for all the gradations are calculated from the expression of the volume of a sphere. Table 2 shows a summary of all these measurements:

Table 2: Summary of all the dimension measurements for the gravel gradations A through E

Gravel Size:		**A**	**B**	**C**	**D**	**E**
Equivalent Radii, R_e [mm]		7.10	5.68	5.60	3.58	1.99
Mean L_1 [mm]		9.99	8.82	8.02	4.21	2.86
Mean L_2 [mm]		16.64	12.75	12.28	7.56	4.62
Mean L_3 [mm]		21.13	18.02	17.69	10.55	7.18
$\frac{L_1}{L_3}$	**Mean**	0.49	0.51	0.46	0.42	0.42
	St. Dev.	0.13	0.16	0.11	0.14	0.13
$\frac{L_2}{L_3}$	**Mean**	0.80	0.73	0.71	0.73	0.67
	St. Dev.	0.12	0.16	0.12	0.15	0.14

To understand how the two aspect ratios vary for each gradation compared to the other one, and to understand whether or not there is some form of geometric similarity across the gradations, $\frac{L_2}{L_3}$ for each gradation is plotted against $\frac{L_1}{L_3}$ and the resulting spread was observed qualitatively. Figure 7 shows the plots obtained for each gradation:

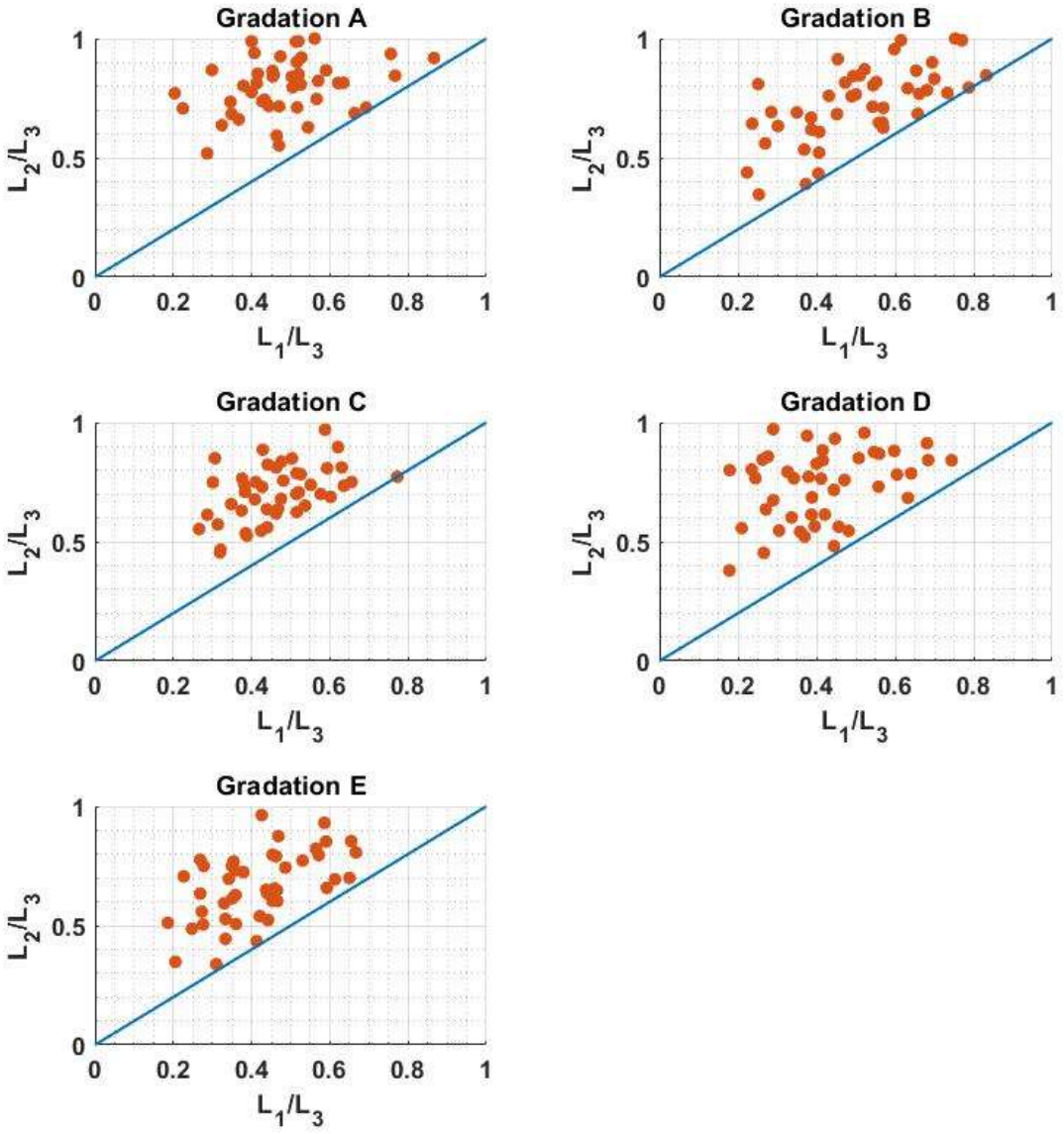

Figure 7: L_2/L_3 vs L_1/L_3 scatter plots showing the distribution of the two aspect ratios for each gradation.

In the figure above (Figure 7), it can be clearly observed that the spreads vary noticeably across the gradations. The spread for gradation C seems to be quite localized compared to the other ones. The ratio $\frac{L_1}{L_3}$ for gradation C seems to lie mostly between 0.25

and 0.7, while $\frac{L_2}{L_3}$ varies between 0.45 and 0.95. The same ratios for other gravels are more spread apart (e.g. $0.2 \leq \frac{L_1}{L_3} \leq 0.85$ and $0.3 \leq \frac{L_2}{L_3} \leq 1.0$ for gradation B). The spreads for A and B can be seen to be more skewed towards the upper right region of the plot. Following histogram plots (Figure 8) obtained from the two ratios for all gradation also illustrate similar observations:

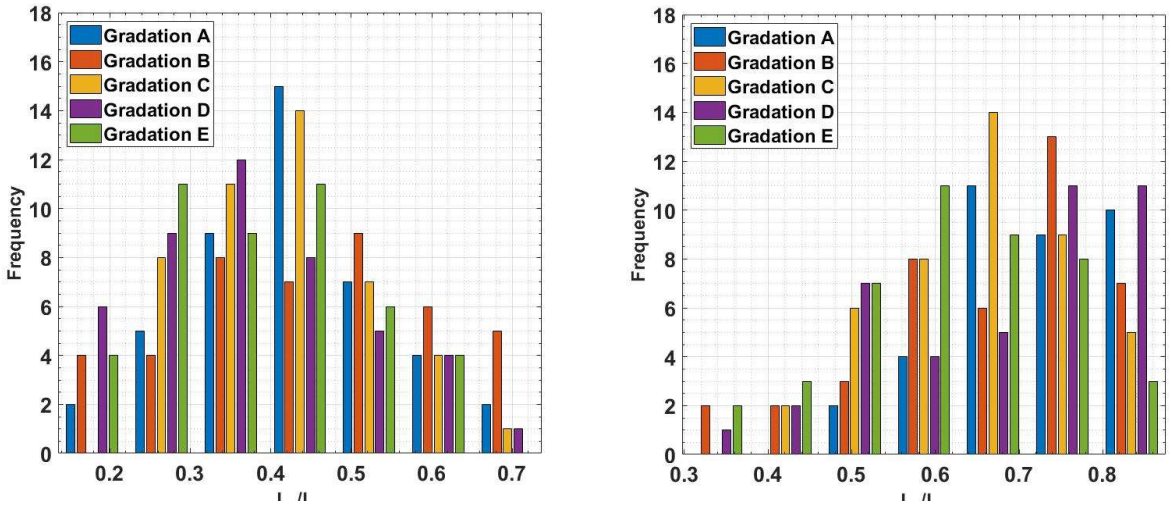

Figure 8: Histograms showing the spread of two aspect ratios (L_1/L_3 and L_2/L_3)

The distribution of $\frac{L_1}{L_3}$ is clearly peaked in the middle with little spread on either side for gradation C, and $\frac{L_2}{L_3}$ has a peak that has a higher frequency than the other gradations which skews towards the right. For both ratios, there are relatively fewer occurrences further away from the peak compared to other gradations which indicates towards a localized spread in Figure 7**.** From this analysis, we can make a qualitative observation that the aspect ratios seem to be different across gradations. This assumption is further checked by performing a single-factor MANOVA (Multivariate Analysis of Variance) from which

we obtained a p-value below the significance level, $\alpha_{sig} = 0.05$, which quantitatively proves that the differences of means across the gradations are statistically significant.

Multivariate Analysis of Variance (MANOVA)

In order to assess the credibility of our qualitative assumption in the previous subsection, multivariate analysis of variance (MANOVA) has been performed (using *IBM SPSS Statistics 27.0* [11]) across the gradations each consisting of two levels of dependent variables namely aspect ratios $\frac{L_1}{L_3}$ and $\frac{L_2}{L_3}$. Single-factor MANOVA is a means of hypothesis testing that tells us, for a number of categories, each having multiple levels of dependent variables, whether the means across the categories have a variation that is statistically significant. This is an extension of ANOVA (Analysis of Variance) where each categorical independent variable only has one level of dependent variable. The underlying assumptions for MANOVA are:

i. Absence of multivariate outliers
ii. Linearity
iii. Absence of multicollinearity
iv. Equality of covariance matrices

Absence of multivariate outliers is checked by assessing the Mahalanobis Distances among the participants. From critical chi-square distribution values at p=0.001, the maximum Mahalanobis Distance is 13.816 for 2 degrees of freedom. Any Mahalanobis Distance beyond this value needs to be removed from the sample, and in our case the maximum Mahalanobis Distance was 9.444, which satisfies the first assumption. The second assumption is linearity among the dependent variables which has been checked by

plotting a scatterplot matrix using *JMP® Pro 14* [12] between the dependent variables (Figure 9). The next assumption is checked by conducting correlations between the dependent variables, and while a moderate correlation is expected, any correlation over 0.80 presents a concern for multicollinearity. We obtained a Pearson's correlation coefficient of 0.468. Equality of covariance matrices is checked by Box's M test, for which the level of significance is typically taken as 0.001, and we obtained a significance level of 0.259. After having met all the mentioned conditions, we performed MANOVA and the following Table 3 summarizes the analysis.

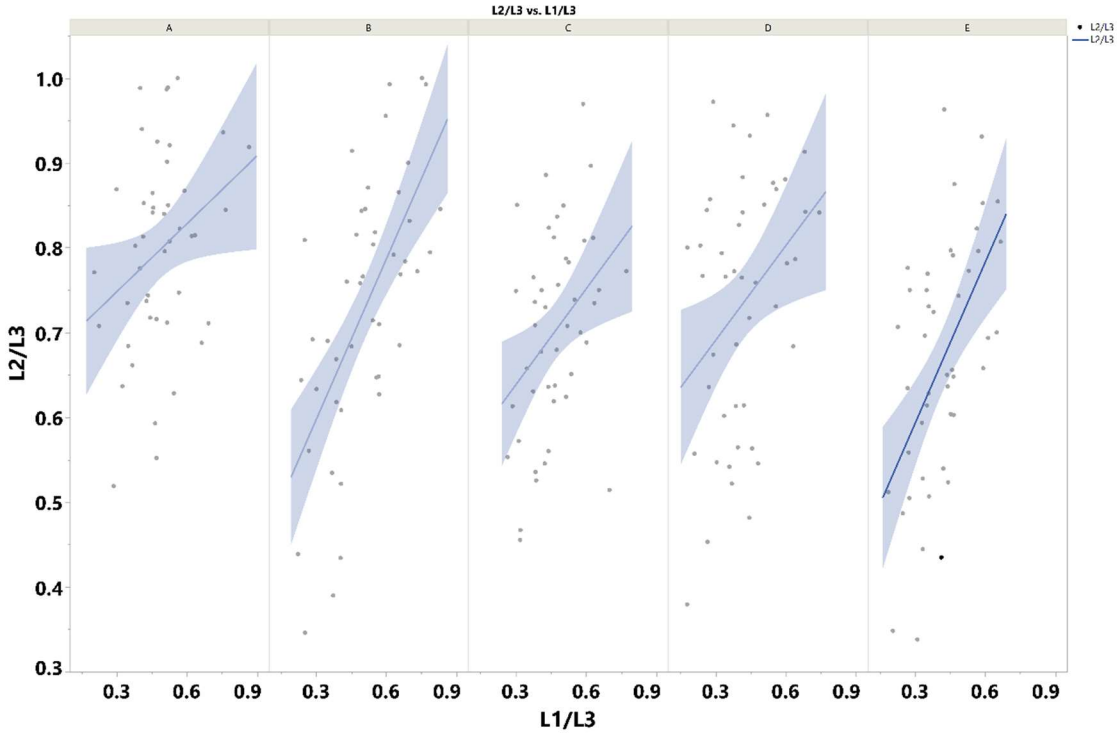

Figure 9: Scatterplot matrix to check linearity between the two dependent variables. (Gradations A-E from left to right)

Table 3: Summary of single-factor multivariate analysis of variance (MANOVA) [11]

Multivariate Tests									
Effect		Value	F	Hypothesis df	Error df	Sig.	η_p^2	Noncent. Parameter	Observed Power
Intercept	Pillai's Trace	.967	3175.96	2.000	219.000	.000	.967	6351.925	1.000
	Wilks' Lambda	.033	3175.96	2.000	219.000	.000	.967	6351.925	1.000
	Hotelling's Trace	29.004	3175.96	2.000	219.000	.000	.967	6351.925	1.000
	Roy's Largest Root	29.004	3175.96	2.000	219.000	.000	.967	6351.925	1.000
Grades	Pillai's Trace	.158	4.70	8.000	440.000	.000	.079	37.629	.998
	Wilks' Lambda	.848	4.69	8.000	438.000	.000	.079	37.502	.998
	Hotelling's Trace	.171	4.67	8.000	436.000	.000	.079	37.376	.998
	Roy's Largest Root	.101	5.53	4.000	220.000	.000	.091	22.134	.976

As shown in Table 3, p-value obtained from the multivariate tests is 0.000 (< 0.05), and Wilk's $\Lambda = 0.848$, which leads us to reject the null hypothesis. A measure of the effect size is given by, $\eta_p^2 = 0.079$, which suggests that nearly 8% of the total variance is accounted for in the population.

In an attempt to observe which of the two levels of dependent variable contribute to a statistically significant difference, a single-factor ANOVA (univariate test) has been performed separately on $\frac{L_1}{L_3}$ and $\frac{L_2}{L_3}$. The results are shown in Table 4 below:

Table 4: Summary of univariate tests

Tests of Between-Subjects Effects									
Source	Dependent Variable	Type III Sum of Squares	df	Mean Square	F	Sig.	η_p^2	Noncent. Parameter	Observ-ed Power
Corrected Model	L1/L3	.31	4	.08	4.12	.003	.07	16.46	.91
	L2/L3	.43	4	.11	5.51	.000	.09	22.06	.98
Intercept	L1/L3	47.37	1	47.37	2497.4	.000	.92	2497.40	1.00
	L2/L3	118.39	1	118.39	6147.2	.000	.97	6147.20	1.00
Grades	L1/L3	.31	4	.08	4.12	.003	.07	16.46	.91
	L2/L3	.43	4	.11	5.51	.000	.09	22.06	.98
Error	L1/L3	4.17	220	.02					
	L2/L3	4.24	220	.02					
Total	L1/L3	51.85	225						
	L2/L3	123.05	225						
Corrected Total	L1/L3	4.49	224						
	L2/L3	4.66	224						

The univariate tests show that, while F_{crit} (4,220)= 2.413, we obtained F(4,220) = 4.12 for $\frac{L_1}{L_3}$ and F(4,220) = 5.51 for $\frac{L_2}{L_3}$, both of which are greater than F_{crit}. The p-values obtained for the said variables (0.003 and 0.000 respectively) are also less than the

significance level, 0.05, which indicates that the null hypotheses for both variables are false. Therefore, the test results suggest that both $\frac{L_1}{L_3}$ and $\frac{L_2}{L_3}$ contribute to the significant difference across the gradations.

CHAPTER THREE

EXPERIMENTAL RESULTS

Observations

During the experiment, the trajectory of each of the dropped gravel piece has been carefully observed. This observation leads us to several findings: each gravel piece rotates during its fall, their path of travel is neither linear, nor vertical and for gravel pieces of same gradation, each piece has a different trajectory than the other. All these findings contradict the underlying assumptions in standard compact debris flight equations. The standard debris flight equations for compact debris treat a compact debris as spherical (Baker 2007 [8], Holmes 2004 [9]) in shape without rotation. This assumption fails to take the aerodynamic moments and lift forces into account which results in a 2D motion of these debris in straight-line wind. The experimental findings, however, show otherwise as seen in a series of frame-by-frame pictures of a gravel drop in Figure 10.

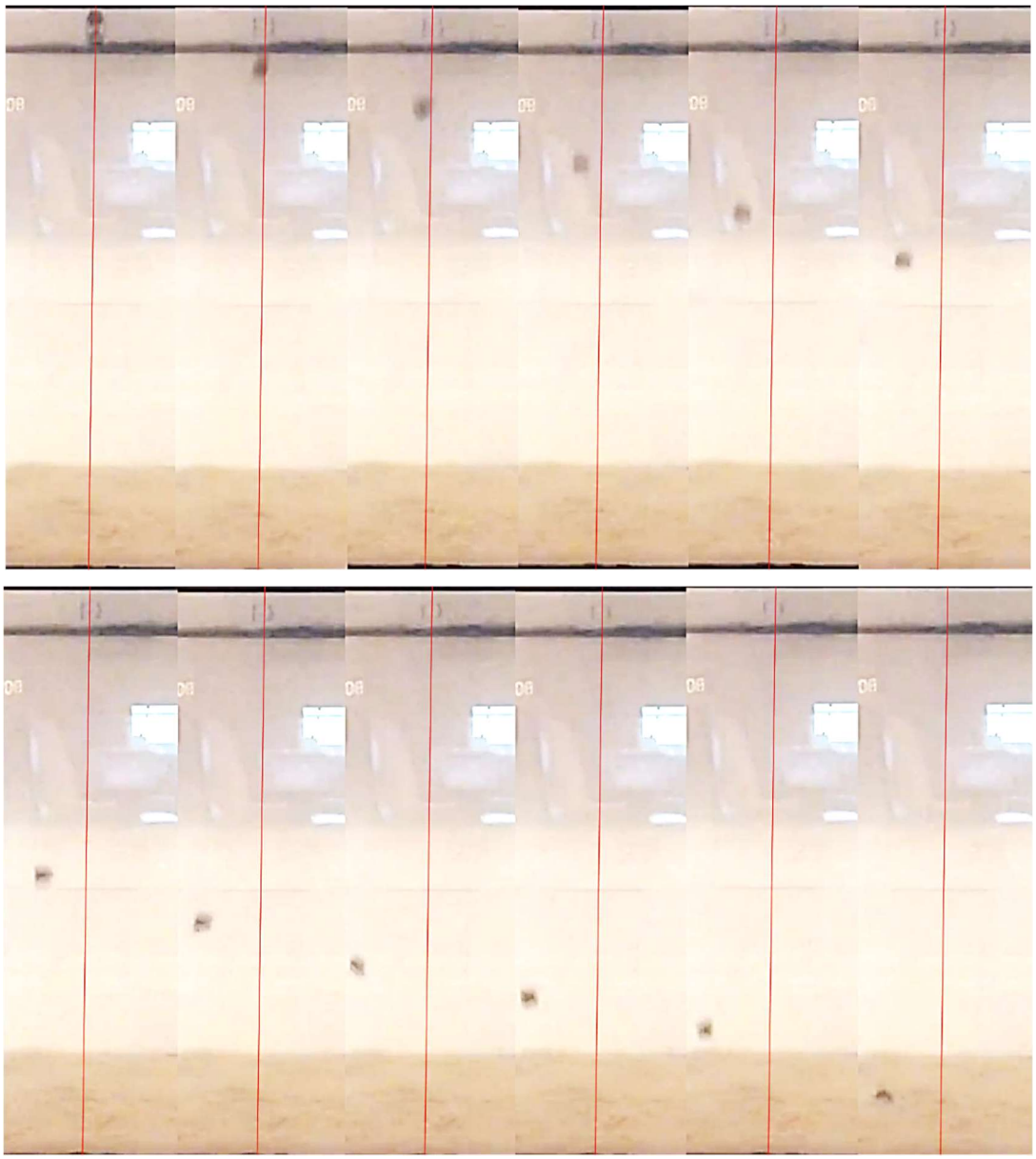

Figure 10: Series of 12 frame-by-frame images, showing a single piece of gravel falling through water. The vertical red lines correspond to the release location.

Initially, as a gravel piece is released from rest, it will fall vertically downwards as long as the only two forces acting on it are weight (vertically down) and buoyancy (vertically up). Since the velocity of the fluid relative to the gravel is vertically upwards at

this point, any subsequent deviation of the piece from vertical is associated with the presence of a lift force acting on it in a direction perpendicular to its velocity at any given point. Moreover, the rotation of gravel pieces during their fall shows that the projected cross-sectional area of the gravel normal to the apparent fluid velocity will continue to vary during the fall. Due to these factors, the resulting landing locations for a number of dropped gravel pieces will be spread around the center of the tank base as shown in Figure 4 in the previous chapter.

The radial distances of these landing locations from center for each gravel gradation are recorded and in Table 5 the means and standard deviations of the radial distances are presented. Figure 11 shows the histogram plot of the radial distances for one gravel gradation (gradation A).

Table 5: Means and standard deviations of radial distances obtained from experiments for all the gradations

Gravel Size:	**A**	**B**	**C**	**D**	**E**
Mean [mm]	56.7	38.9	52.8	48.6	30.1
St. Dev. [mm]	30.0	28.5	32.2	30.8	22. 3

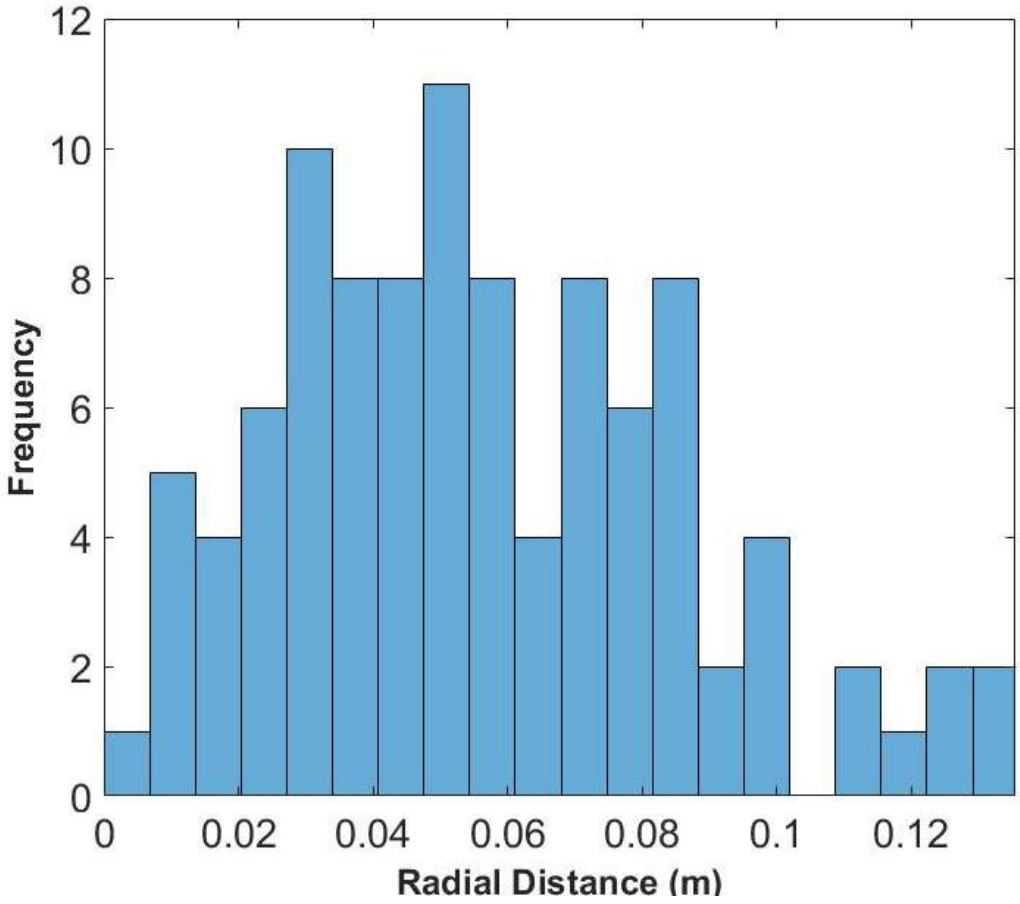

Figure 11:Histogram of radial distances of landing locations for gradation A.

From the histogram in Figure 11, we observe that the peak has a finite non-zero value. This implies that only very few pieces actually land directly below the release point, rather in most cases, the path traveled by the dropped gravel pieces are not vertical. This is qualitatively similar to the drop experiments of Tohidi & Kaye (2017) [13] for rod-like debris.

CHAPTER FOUR

MODEL DEVELOPMENT

This section describes the development and optimization of a stochastic compact debris flight model that accounts for variation in gravel geometry, variation in orientation during flight, and lift forces generated from asymmetry in the gravel shape and rotation during flight.

Model Equations

In order to develop a 3-D debris trajectory model, it is necessary to define a fixed system of coordinates to track the motion of gravels in 3-D space. Figure 3 shows the fixed, right-handed coordinate system that has its origin placed at the release point for the experiments and the same coordinate system is used in the model development. The position and velocity vectors for the center of a given gravel piece are given by the position $\boldsymbol{x} = [x, y, z]$ and velocity, $\boldsymbol{u} = [u_x, u_y, u_z]$ respectively. While the gravel pieces are observed to rotate during their fall the model assumes that the rotation only contributes to changes in the magnitude of the drag force (through changes in cross-sectional area and C_D) and the magnitude and direction of the lift force. As the drag and lift forces are modelled stochastically there is no need to explicitly model the aerodynamic moments and resulting rotation.

The equations that govern the motion of these particles are the rectilinear equations of motion in three dimensions:

$$\frac{d^2\boldsymbol{x}}{dt^2} = \frac{d\boldsymbol{u}}{dt} = \frac{\boldsymbol{F_w} + \boldsymbol{F_B} + \boldsymbol{F_L} + \boldsymbol{F_d}}{m} \tag{3}$$

where bolded symbols represent Cartesian vectors, and the velocity vector ($\boldsymbol{u}$) is given by

$$\frac{d\boldsymbol{x}}{dt} = \boldsymbol{u} \tag{4}$$

and m is the mass of the gravel piece. The forces acting on the gravel are the drag force

$$\mathbf{F_d} = -\left(\frac{1}{2}\rho A|\boldsymbol{u}|\boldsymbol{u}C_D\right), \tag{5}$$

lift force,

$$\mathbf{F_L} = \left(\frac{1}{2}\rho A|\boldsymbol{u}|^2 C_L\right)\boldsymbol{n_L}, \tag{6}$$

weight,

$$\mathbf{F_w} = (0,0,-mg), \tag{7}$$

and buoyancy force,

$$\mathbf{F_B} = (0,0,\rho\forall g). \tag{8}$$

Herein ρ is the density of fluid, A is a characteristic cross-sectional area for the gravel, C_D and C_L are drag and lift coefficients respectively, g is acceleration due to gravity, $\forall$ is a characteristic volume the gravel and $\boldsymbol{n_L}$ is a unit vector in the direction of lift force. See Figure 12 for the kinematic and free body diagrams. Solving the coupled equations (3) and (4) leads to the velocity and position of the gravel piece as a function of time.

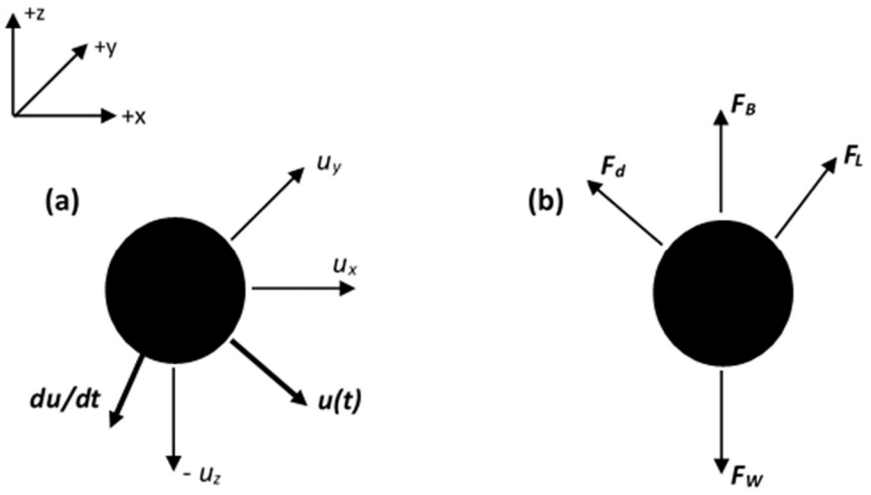

Figure 12:(a) Velocity diagram showing the velocity components in x, y and z directions. (b) Free body diagram.

Model Parameters

However, for any given collection of gravel pieces, even if from the same gradation, the values of A and ∀ will vary from piece to piece. During flight, changes in orientation mean that the area normal to the apparent fluid velocity will vary over time. Changes in orientation will also lead to variation in the force coefficients C_D and C_L and the direction of the lift force $\boldsymbol{n_L}$. Finally, the initial values of all these parameters will vary depending on the orientation of the gravel upon release from rest. It is highly likely that, even if all these parameters were known explicitly as a function of orientation, it would not be possible to predict the trajectory as the results would be so sensitive to the initial release angle that, in the absence of perfect knowledge of the release, it would not be possible to predict an individual flight path [13]. Therefore, the model development is focused on predicting the statistical properties of a large number of trajectories for gravel pieces

released under nominally identical conditions. To do this, A, C_D, C_L and $\boldsymbol{n_L}$ are treated as randomly varying parameters in the model.

The ranges, within which C_d and C_L are varied in this study, are determined based on the work of Chai et al. (2019) [14] whose measurements showed values of C_D and C_L vary over the ranges $0.4 < C_D < 0.8$ and $-0.2 < C_L < 0.2$ respectively for a range of different rock pieces oriented in different directions. Given that the force coefficients are functions of an unknown orientation and have no knowledge of the distribution of orientation during flight, we assume that they are both uniformly distributed between the limits given.

The area A was taken to have a reference value given by

$$A_R = \pi R_e^2 \tag{9}$$

where, R_e is the equivalent radius of the average gravel piece in a given gradation. It is the radius of the sphere that has the same volume as the average gravel piece. The range of possible areas is taken to be

$$\overline{L_1}\,\overline{L_2} \leq A \leq \overline{L_2}\,\overline{L_3} \tag{10}$$

where $\overline{L_1}, \overline{L_2}$, and $\overline{L_3}$ are the averages of the shortest, intermediate, and longest gravel dimensions respectively as defined in chapter 2. This area calculation assumes that the gravel is cuboid and will, therefore, overestimate the areas. However, this overestimation is offset by using the average length values such that there will be gravel pieces for which $\overline{L_1}\,\overline{L_2}$ and $\overline{L_2}\,\overline{L_3}$ are outside the bounds assumed for A. The area value used in the model is

$$A = \alpha A_R \tag{11}$$

where, α is a random variable uniformly distributed over the range

$$\frac{\overline{L_1}\,\overline{L_2}}{A_R} \leq \alpha \leq \frac{\overline{L_2}\,\overline{L_3}}{A_R} \tag{12}$$

As the model does not calculate orientation, the direction of the lift force is only known to be normal to the apparent fluid velocity. However, this criterion only identifies the plane normal to the velocity vector. A specific unit vector, $\boldsymbol{n_L}$, is, therefore, generated by first defining a reference unit vector ($\boldsymbol{n_{ref}}$) in the global x-y plane

$$\boldsymbol{n_{ref}} = (sin\theta, cos\theta, 0) \tag{13}$$

in which θ is randomly generated at the start of each flight from a uniform distribution over the range $0 \leq \theta < 2\pi$. The unit vector normal to the direction of the apparent fluid motion is calculated by taking the cross product of the unit vector in the direction of the velocity with the reference unit vector

$$\boldsymbol{n_L} = \frac{\boldsymbol{u}(t)}{|\boldsymbol{u}(\boldsymbol{t})|} \times \boldsymbol{n_{ref}} \tag{14}$$

Therefore, the lift force vector in three dimensions takes the following form:

$$\mathbf{F_L} = \left(\frac{1}{2}\rho_f A|\boldsymbol{u}|\boldsymbol{u}C_L \times \boldsymbol{n}_{ref}\right) \tag{15}$$

The coupled governing differential equations (3) and (4) are numerically solved in *MATLAB* using a 4th order Runge-Kutta method with fixed time-step. The numerical integration is performed under the initial conditions **x(t=0)**=[0, 0, 0] and **u(t=0)**=[0, 0, 0], and the boundary condition $z = z_{max}$ at $t = t_{final}$, where z_{max} is the depth of tank. As the time taken to reach z_{max} is unknown for any given release, the equations are integrated for a large enough time that the particle has dropped further than z_{max} and the time at

which z_{max} is reached, along with the location vector $\boldsymbol{x} = [x, y, z_{max}]$, is calculated by interpolating the trajectory data on to $z = z_{max}$.

At the beginning of each simulation the initial values of the random variables C_D, C_L, α and $\boldsymbol{n_{ref}}$ are randomly generated from the distributions described above. Then, at the end of each time-step, the values are randomly perturbed before the next time-step in the integration. To avoid a drastic change in the magnitude of each of these parameters (e.g. α), the new values are generated randomly from a continuous uniform distribution over a prespecified range ($\pm\delta\alpha$) about the previous value. So, the new values of C_D, C_L, θ and α are generated randomly from $\pm\,\delta C_D$, $\pm\,\delta C_L$, $\pm\,\delta\theta$ and $\pm\,\delta\alpha$ ranges about the previous values of the corresponding parameters. To illustrate the idea, consider the case where the value of C_D from the previous timestep was 0.55 and δC_D has a fixed value of 0.03 for that simulation. Then, the new value of C_D for the next time step, for this case, will be randomly generated from a uniform distribution between $C_D - \delta C_D$ and $C_D + \delta C_D$, or 0.52 and 0.58 for this example. The same perturbation approach is used for C_L, θ and α.

These random perturbations of C_D, C_L, α and θ at each time-step are to account for changes in orientation that alter the projected area ($\delta\alpha$), the magnitude of the drag and lift forces (δC_D and δC_L) and the direction of the lift force ($\delta\theta$). Over the course of a given set of flight simulations, the statistical distribution of the gravel landing locations will depend on the magnitude of the perturbations (δC_D, δC_L, $\delta\alpha$ and $\delta\theta$) and the number of times that the values are perturbed ($N = T/\delta t$) where T is the time taken to reach $z = z_{max}$ and δt is the integration time-step. To minimize the number of model parameters, the time-step was fixed for all simulations and was taken to be the time taken for the equivalent sphere

to fall one radius when traveling at its terminal velocity. The terminal velocity was calculated using the median value of the $C_D = 0.6$ to yield

$$U_T = \sqrt{\frac{2(F_w - F_B)}{0.6\rho A_e}} \tag{16}$$

The time-step is, therefore,

$$\delta t = \frac{R_e}{U_T} \tag{17}$$

Therefore, the time scale is characteristic of a typical gravel piece within a given gradation and is consistently defined over all gradations.

The ranges of C_D, C_L, and α are determined from laboratory measurements of gravel geometry and wind tunnel measurements of the force coefficients. The equivalent sphere properties (m and R_e) are also calculated from measurement data. Therefore, the only unknown parameters in the model are δC_D, δC_L, $\delta\alpha$ and $\delta\theta$. These four parameters are used as fitting parameters to match the simulated landing locations with the experimental data.

CHAPTER FIVE

MODEL RESULTS AND COMPARISON WITH EXPERIMENTS

Model Results and Comparison

The numerical studies were carried out for different combinations of the four fitting parameters discussed in previous chapter. The perturbation ranges $\delta C_D, \delta C_L$ and $\delta\alpha$ were varied from 0 to 50% of the overall range of the respective parameter in increments of 2.5% of the overall range while $\delta\theta$ was varied from 0 to 30° in 1.5° increments. This leads to a total of 21 values for each perturbation parameter. To capture all possible combinations of these four parameters, a total of 21^4 simulations were run for each drop. This resulted in a total of more than 94.25 million simulations of drops for five gravel sizes and 100 drops per gravel size. The numerical results for each combination of parameters were, then, compared to the experimental measurements in chapter 3. For each gradation, the set of fitting parameters that yields the minimum error was extracted as an optimum set of model parameters. To show how the other combinations yield less desirable results compared to the optimized combination of the parameters, Figure 13 shows the resulting spread of landing locations for the largest gravel size (gradation A) as a scatter plot and the ranked radial distances obtained from the model are plotted against the ranked experimental radial distances. The solid red line has a slope of 1 representing a perfect agreement between the experiments and the model. Both these plots are based on the worst set of model parameters.

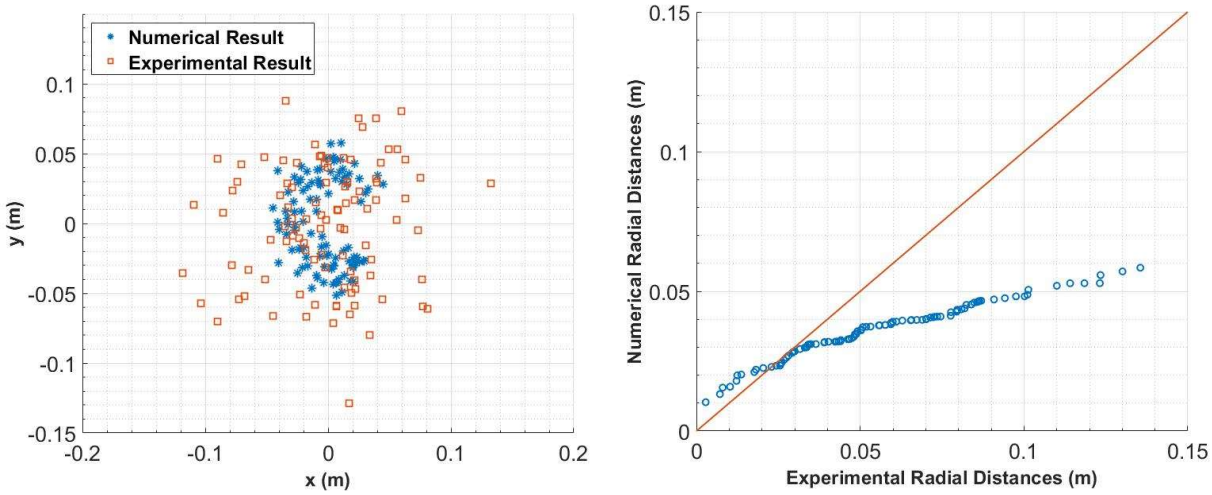

(a) (b)

Figure 13: (a) Spread of landing locations obtained from the model in comparison with experimental spread (b) Comparison of radial distances obtained from model with respect to experimental radial distances. (Both plots are based on worst combination of perturbation parameters for Gradation A)

It is clear from this set of plots (Figure 13) that the spread obtained from the model does not resemble the experimental spread at all.

Optimization Technique

For all the combinations of fitting parameters, the numerical simulations give us the x and y coordinates of landing locations for one hundred drops per gravel size. The radial distances of each landing location from the center of the tank can be easily calculated from the coordinates, from which the mean and the standard deviation of the radial distances are calculated. To find an optimized combination of $\delta C_D, \delta C_L, \delta\theta$ and $\delta\alpha$, the absolute differences between the two means (numerical and experimental) and the two standard deviations are calculated. These two quantities are not to be minimized

independently since they are not exclusive of each other. For example, a very localized spread (meaning the standard deviation is smaller) can yield a mean which can be same as another spread that is less localized (i.e. with higher standard deviation). To optimize both these quantities, an optimization parameter (ε) is introduced, which is defined in equation (18) below as the square root of the sum of the squares of the differences between the means and the differences between the standard deviations.

$$\varepsilon = \sqrt{(\bar{r}_{exp} - \bar{r}_{numerical})^2 + (\sigma_{r(\exp)} - \sigma_{r(numerical)})^2} \tag{18}$$

where, $\bar{r}$ is the mean and σ_r is the standard deviation of the radial distances. The optimized set of $\delta C_D, \delta C_L, \delta\theta$ and $\delta\alpha$ is obtained for the case where ε is minimum.

Below, the optimized combination of $\delta C_D, \delta C_L, \delta\theta$ and $\delta\alpha$, their resulting means and standard deviations of radial distances and the experimental means and standard deviations of radial distances are shown in Table 6 for each gravel size.

Table 6: Optimized combinations of the perturbation parameters and the resulting means and standard deviations obtained from the model for all gradations

	Gravel Sizes				
	A	B	C	D	E
δC_D	0.13	0.04	0.02	0.01	0.10
δC_L	0.000	0.000	0.005	0.000	0.005
$\delta\theta$ (degrees)	6.00	28.50	4.50	18.00	27.00
$\delta\alpha$ (% of $\alpha_{max} - \alpha_{min}$)	0.1170 (10%)	0.5488 (47.5%)	0.0894 (7.5%)	0.1486 (12.5%)	0.5642 (35%)
Experimental Mean Radial Distance (mm)	56.7	38. 9	52.8	48.6	30.1
Numerical Mean Radial Distance (mm)	56.8	38.8	52.8	48.6	30.0
Experimental St. Dev. (mm)	30.0	28.5	32.2	30.8	22.3
Numerical St. Dev. (mm)	30.0	28.6	32.2	30.9	22.3
Optimization Parameter, ε (m)	5.67×10^{-5}	1.10×10^{-4}	4.39×10^{-5}	5.58×10^{-5}	3.35×10^{-5}

From the summary presented in Table 6, we can see that for optimized condition, δC_L has zero or near zero values. This indicates that according to this model, the trajectory of the dropped gravel pieces depends mostly upon the initial lift coefficient for each drop, and during the drop, the variation of C_L appears to have minimal impact on the landing location. All the other parameters however seem to have noticeable variation across the gradations, which is expected since the different gradations are not geometrically similar as discussed in chapter 2. In Figure 14(a) below, the spread of landing locations obtained

from the optimized combination of $\delta C_D, \delta C_L, \delta\theta$ and $\delta\alpha$ is shown with the experimental spread as a scatter plot for gradation C. Figure 14(b) shows a comparison between the ranked radial distances (experimental and numerical) of landing locations for the same case. A solid red line shows the line of 100% agreement between the experimental and numerical data points.

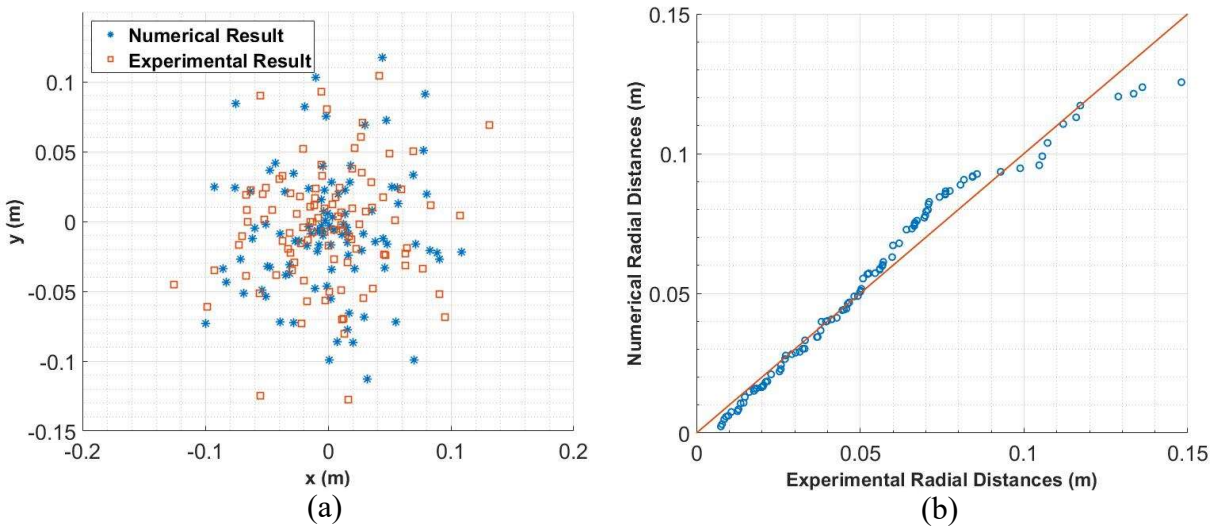

(a) (b)

Figure 14: (a) Spread of landing locations obtained from the model in comparison with experimental spread, (b) Comparison of radial distances obtained from model with respect to experimental radial distances. (Both plots are based on the optimized combination of perturbation parameters for Gradation C)

In Figure 15 below, the comparison of experimental and numerical radial distances obtained from the optimized combination of perturbation parameters for each gravel gradation are shown:

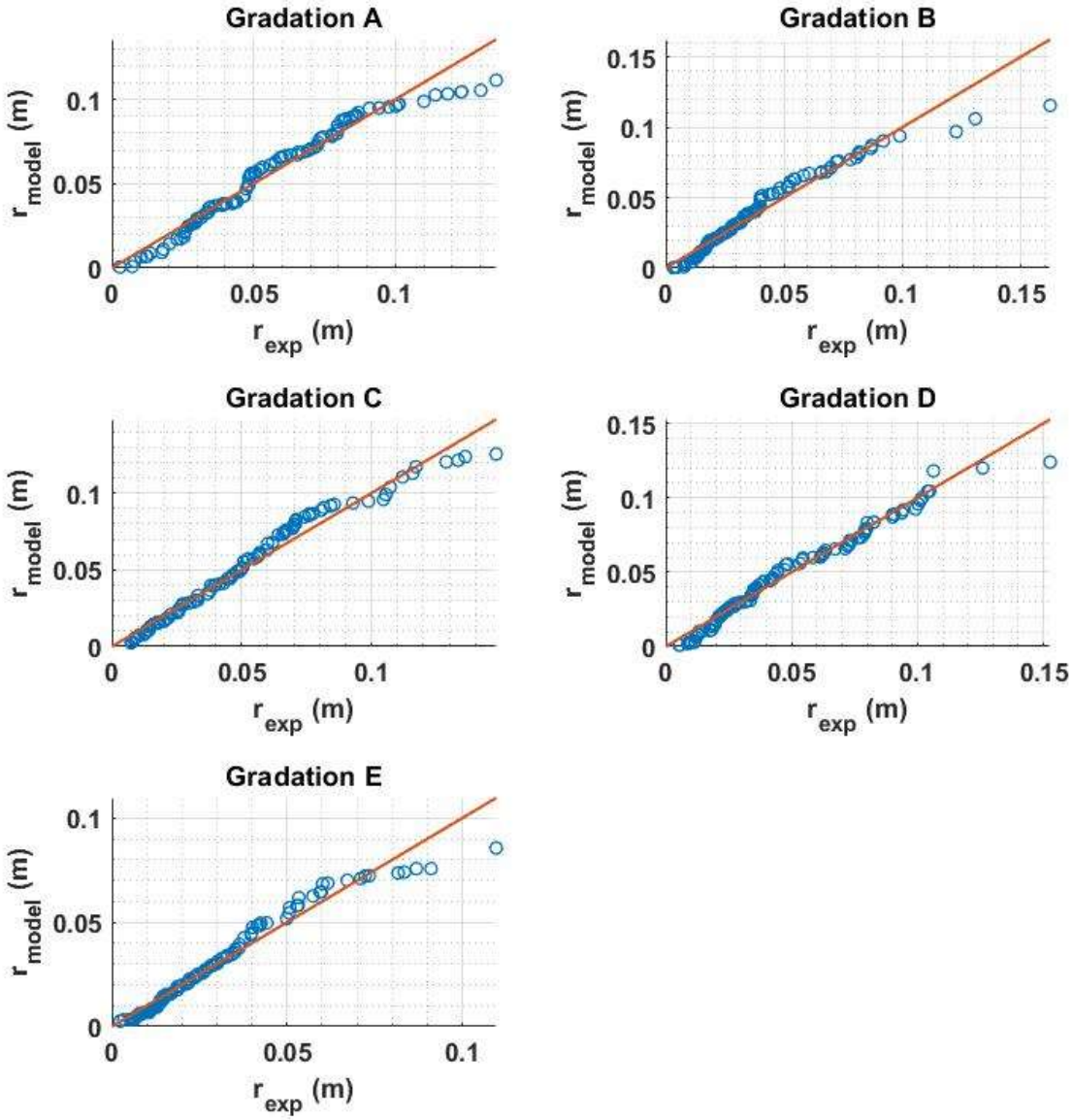

Figure 15: Comparison between numerical and experimental radial distances.

Figure 15 shows that for the optimized model, the numerical data are in good agreement with the experiments except at the tail for large values of radial distances (r). The model consistently underestimates the top 3-6% at the top and fails to capture the really extreme events.

To understand how the optimization parameter (ε) varies near the optimized set of fitting parameters, contour plots are generated for ε keeping two of the parameters fixed at a time while varying the other two as shown in Figure 16.

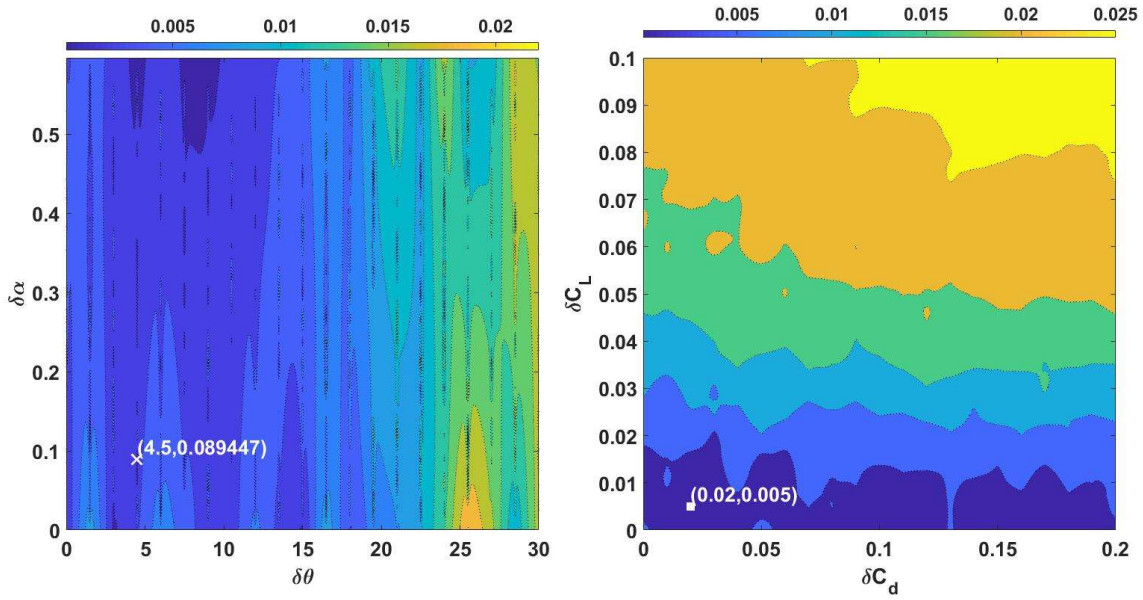

Figure 16:Contour plots showing variation of optimization parameter (ε) with two perturbation parameters at a time while the other two are kept fixed at their optimized values. (Gradation C)

From Figure 16, the optimization parameter (ε) appears to have a smooth gradient towards its optimized value. However, since ε varies over several orders of magnitudes, the contour plots here cannot capture the gradient properly near the minimum as indicated by large blue regions near the minimum. From Figure 17 below, where we plot $\log_{10}\varepsilon$ to generate similar contours, we can see that near the optimized condition, ε reduces monotonically. A thin blue band on the left figure near the minimum ε indicates that for this gradation, ε is quite sensitive to $\delta\theta$. On the right-hand side figure, however, near the minimum, ε appears to have a smooth gradient.

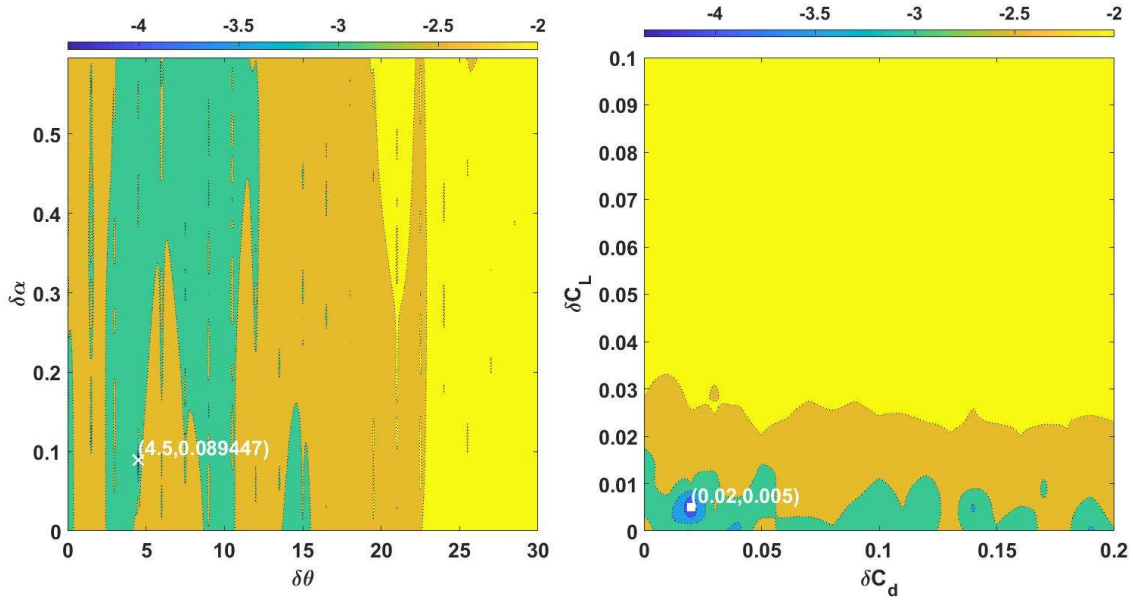

Figure 17: Contour plots showing variation of logarithm of optimization parameter ($\log_{10}\varepsilon$) with two perturbation parameters at a time while the other two are kept fixed at their optimized values. (Gradation C)

Global Optimization Criteria

In an attempt to optimize the entire system globally, we introduce a global optimization parameter (ε_g). To do that, we take the sum of squared optimization parameters (ε) [equation (18)] for each combination of perturbation parameters across all five gradations and then take a square-root of the sum as shown in equation (19).

$$\varepsilon_g = \sqrt{\sum_{i=A}^{E} \varepsilon_i^2} \tag{19}$$

The globally optimized combination of the perturbation parameters is then characterized by a minimum value of ε_g. Table 7 below shows the combination of parameters and their results for all five gradations.

Table 7: Mean and standard deviation of the radial distances obtained from the model under globally optimized condition [1]

	Gravel Sizes				
	A	**B**	**C**	**D**	**E**
$\delta\alpha$	0.3509	0.3466	0.3578	0.3565	0.4836
Experimental Mean Radial Distance (mm)	56.7	38. 9	52.8	48.6	30.1
Numerical Mean Radial Distance (mm)	51.0	39.9	48.7	45.3	36.5
Experimental St. Dev. (mm)	30.0	28.5	32.2	30.8	22.3
Numerical St. Dev. (mm)	27.6	25.2	28.3	28.0	23.9
Individual Optimization Parameter, ε_g (m)	0.0062	0.0035	0.0056	0.0044	0.0066
Global Optimization Parameter, ε_g (m)	0.0121				

1. Globally optimized perturbation parameters: $\delta C_D = 0.09$, $\delta C_L = 0.005$, $\delta\theta = 21°$ *and* $\delta\alpha = 30\%$ *of* $(\alpha_{max} - \alpha_{min})$.

From Table 7, we observe that the entire system is globally optimized for a low value of δC_L, which indicates, as we have discussed before, the model offers the best prediction when the alteration of lift coefficient (C_L) is very minimal compared to the initial lift coefficient. The relatively large value of $\delta\theta$, however, suggests that during the drop, the orientation of the gravel pieces keeps altering noticeably, as is our observation from videos of experiments (Figure 10).

In Figure 18 below, the landing locations for gradation C under the globally optimized condition is shown on the left-hand side with experimental spread, and on the right-hand side, the ranked numerical and experimental radial distances are shown, with solid red line indicating a hundred percent agreement between the model and experiment.

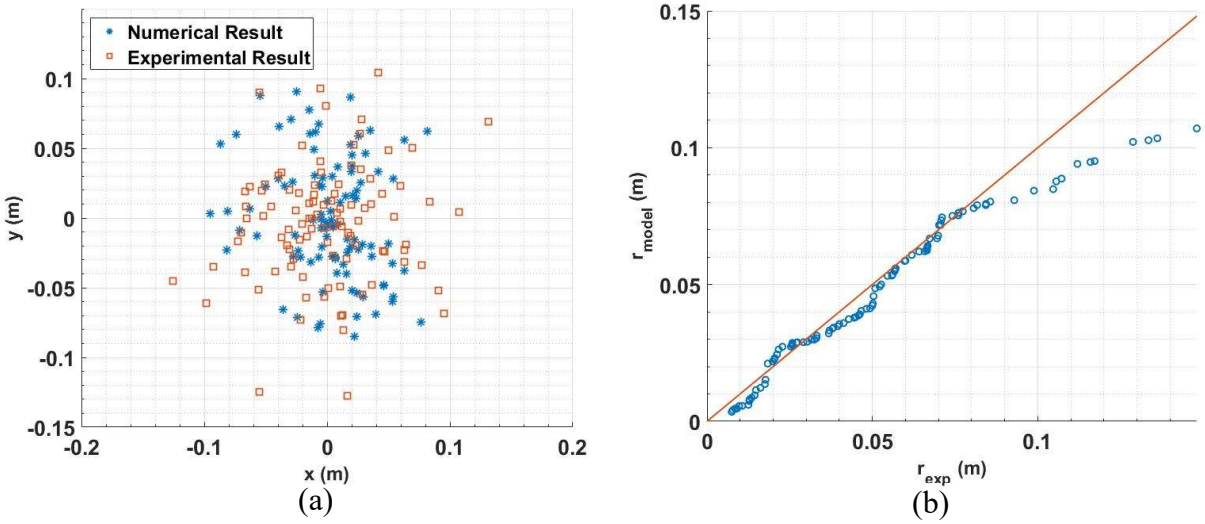

Figure 18: (a) Spread of landing locations obtained from the model in comparison with experimental spread, (b) Comparison of radial distances obtained from model with respect to experimental radial distances. (Both plots are based on the globally optimized combination of perturbation parameters for Gradation C)

Figure 18 shows that under the globally optimized condition for gradation C, the model loses its accuracy to some extent compared to individual optimization and the prediction error towards the tail of radial distance distribution increases. This is in part due to the violation of the experimental condition of geometric similarity. A more holistic picture can be observed in following Figure 19, where the ranked numerical and experimental radial distances are compared for all gradations under the globally optimized condition.

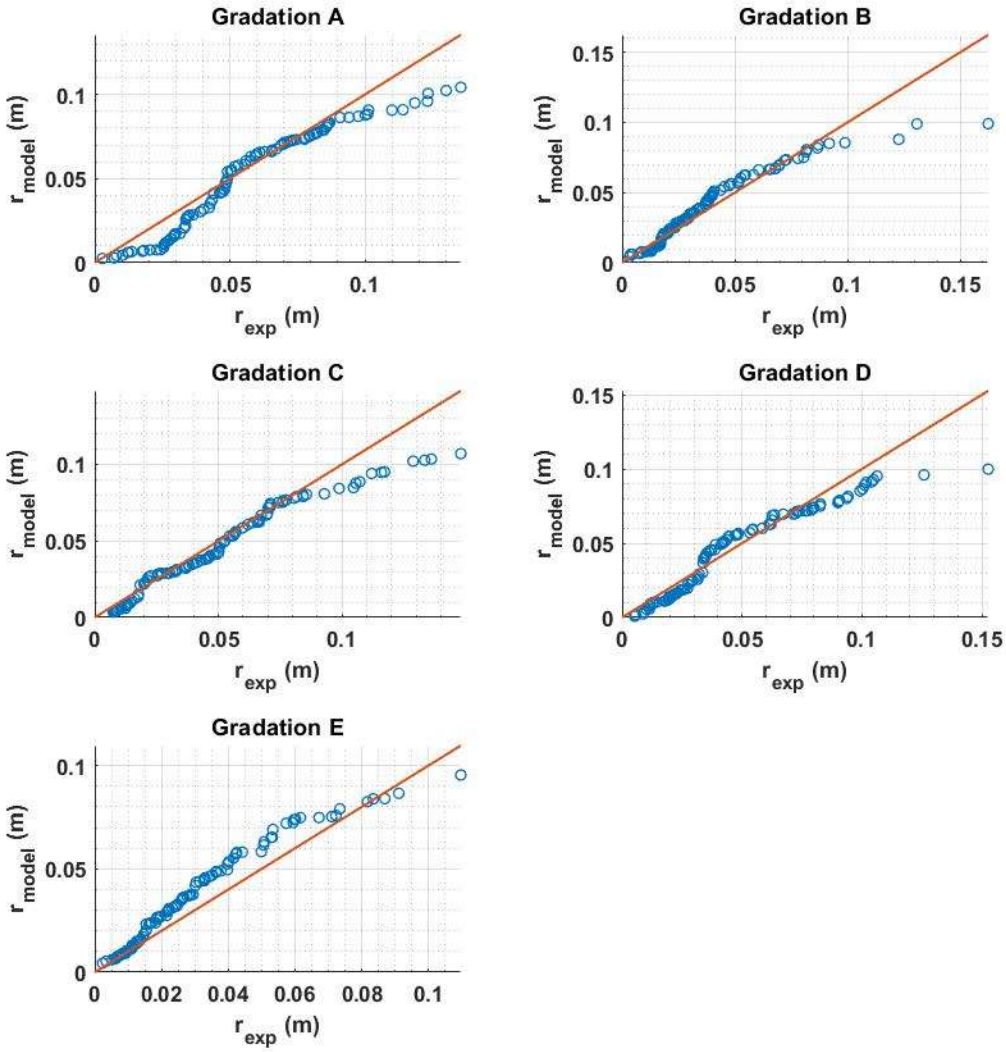

Figure 19: Comparison between numerical and experimental radial distances for all gradations (Based on global optimization)

From Figure 19 we can see that under the globally optimized condition, the model predicts the radial distances with a reduced accuracy compared to the individually optimized cases. While the model under predicts the distances of landing locations for the largest gravel gradation (A), for three middle gradations (B, C and D), the prediction in the

middle and lower end of the distribution are reasonable with an increased rate of under prediction at the tail. For the smallest gradation (E), however, the tail region is resolved better at the expense of an over prediction in the middle and lower-middle region of the radial distance distribution.

CHAPTER SIX

DISCUSSION AND CONCLUSIONS

Review and Conclusion

In an attempt to address the shortcomings of standard equations of motion for compact debris, this study develops a numerical model that takes alteration of various factors during the drop of such debris into account. Due to the underlying assumption of compact debris being spherical in shape in the standard equations, the effects of change in projected area, drag and lift coefficients and initial release angle throughout a single drop cannot be captured. However, from the experiments discussed in chapter 2, it can clearly be observed that the said factors play an important role during the travel of each individual particle. Based on the experimental findings discussed in chapter 3, we adjusted several parameters that offers the best agreement of the model data with the experiments. The four fitting parameters that are used to fit the model to the experiments are the amounts by which drag and lift coefficients (C_D and C_L), initial release angle (θ) and the area coefficient (α) are varied throughout a single drop after each time step for numerical integration. On an individual level, the model offers the best fit at different combinations of these parameters for different gradations of gravels which is expected since the gradations are not geometrically similar as discussed in chapter 2.

Under its optimized condition, the model presents reasonable agreement with the experiment for most of the drops, however, it consistently fails to capture the extreme events at large radial distances and under predicts the top 3-6% of the radial distances of

landing locations. We optimized the model globally across all experiments for all gradations to obtain one optimum combination of the fitting parameters for all gradations. For that case the model appears to present a reduced accuracy overall, with an increased rate of under prediction of radial distances mostly towards the tail of the distribution. One possible explanation for this underestimation at the tail is that the overall range of C_L we used ($-0.2 < C_L < 0.2$) while developing the model in this study may have been too narrow. Since the deviation of dropped gravel pieces from a vertical trajectory is associated with the effect of lift force acting on them, expansion of the range of C_L values can be an approach to see if the model can capture the tail of the distribution better. We have also observed that during the motion of each individual gravel piece, the C_L appears to vary slightly (as indicated by low value of δC_L under optimized condition) according to the model, while there is a significant variation in its orientation throughout the drop. Finally, we have observed that the optimization parameter (ε), although being quite sensitive to the fitting parameters, has a smooth gradient near its minimum value.

Future Research

This study addresses the motion of compact debris in stagnant environment, which is never the scenario in practical cases. Investigations are required to obtain a more precise understanding of the motion of debris in an ambient wind flow. However, transition to air is associated with increased relative magnitude of weight force due to the absence of significant buoyancy force. This increase in magnitude of vertical force needs to be accounted for in time-step consideration. There are scopes of improvement in the proposed stochastic model. As shown in this study, when the model is optimized for all five

gradations globally, the overall accuracy reduces. This reduction of accuracy can be attributed to the fact that the gravel gradations used in this study are not geometrically similar. Therefore, one optimization scheme applied globally to all five gradations is expected to come at an expense of accuracy compared to the individual optimizations. This can be addressed by modifying the fitting parameters used in this study by relating them back to the geometric properties of the gravel across their gradations. The model, optimized based on the modified fitting parameters, can then be expected to present a more generalized set of results for all five gradations with better accuracy. Upon ensuring a more accurate fit in all ranges of radial distances for all gradations, this model can be expanded to investigating the motion of debris in ambient wind flow by making adjustments to the time-step considerations as recommended above. Later the behavior of the model in the presence of external wind field can be compared with respect to the physical findings from wind tunnel experiments.

Gaining a thorough understanding of the motion of windborne debris can bring great benefit for us to reduce the impact of such debris during extreme wind events. From accurate predictions of landing locations of flying debris and missiles, we can take preemptive measures to reduce the overall loss of property and lives in case of such extreme events.

Appendix A

Fourth-Order Runge-Kutta Methods

The model presented in this study solves the coupled equations of motion (3) and (4) to obtain the position and velocity vectors of each dropped gravel piece. The numerical method to solve the said differential equations used in this study is a fourth-order Runge-Kutta method. Runge-Kutta methods are a family of single-step, explicit, numerical techniques for solving first-order ordinary differential equations. For a step size of $h = x_{i+1} - x_i$, the value of dependent variable at (i+1)th step is given by:

$$y_{i+1} = y_i + slope.h \qquad A1$$

where *slope* is constant. The value of *slope* is calculated at several points within the interval h and the number of points that are used for determining the value of *slope* within that interval is how different orders of Runge-Kutta methods are classified. The accuracy of the method increases (i.e. truncation error decreases) with increasing order. In this section, we will briefly discuss the method. (Gilat and Subramaniam, 2008) [15]

For a differential equation, given by $\frac{dy}{dx} = f(x, y)$, the equations for classical fourth-order Runge-Kutta method are:

$$y_{i+1} = y_i + \frac{1}{6}(K_1 + 2K_2 + 2K_3 + K_4)h \qquad A2$$

where,

$$K_1 = f(x_i, y_i)$$

$$K_2 = f\left(x_i + \frac{h}{2}, y_i + K_1\frac{h}{2}\right)$$

$$K_3 = f\left(x_i + \frac{h}{2}, y_i + K_2\frac{h}{2}\right) \qquad A3$$

$$K_4 = f(x_i + h, y_i + K_3 h)$$

Using the known initial value, $f(x_i, y_i)$ at $x = x_i$, all the coefficients in equation A3 are calculated to solve for y_{i+1} from equation A2. The calculated x_{i+1} and y_{i+1} will be the initial values for $(i+2)^{th}$ step and so on.

References

[1] J. E. Minor, "Lessons Learned from Failures of the Building Envelope," *Journal of Architectural Engineering,* vol. 11, no. 1, pp. 10-13, 2005.

[2] T. L. Smith and J. R. McDonald, "Roof Wind Damage Mitigation: Lessons from Hugo," in *Hurricane Hugo One Year Later*, Charleston, SC, 1990.

[3] P. R. Sparks, S. D. Schiff and T. A. Reinhold , "Wind damage to envelopes of houses and consequent insurance losses," *Journal of Wind Engineering and Industrial Aerodynamics,* vol. 53, no. 1-2, pp. 145-155, 1994.

[4] A. Kareem, in *Hurricane Alicia: One Year Later*, Galveston, Texas, 1985.

[5] R. A. Behr and J. E. Minor, "A survey of glazing system behavior in multi-story buildings during Hurricane Andrew," *The Structural Design of Tall Buildings,* vol. 3, no. 3, pp. 143-161, 1994.

[6] N. H. C. (NOAA), "Hurricanes in History," U. S. Department of Commerce, [Online]. Available: https://www.nhc.noaa.gov/outreach/history/. [Accessed 09 Nov 2020].

[7] J. A. B. Wills, B. E. Lee and T. A. Wyatt, "A model of wind-borne debris damage," *Journal of Wind Engineering and Industrial Aerodynamics,* vol. 90, no. 4-5, pp. 555-565, 2002.

[8] C. J. Baker, "The debris flight equations," *Journal of Wind Engineering and Industrial Aerodynamics,* vol. 95, no. 5, pp. 329-353, 2007.

[9] J. Holmes, "Trajectories of spheres in strong winds with application to wind-borne debris," *Journal of Wind Engineering and Industrial Aerodynamics,* vol. 92, no. 1, pp. 9-22, 2004.

[10] "ScanIt," AmsterCHEM, [Online]. Available: https://www.amsterchem.com/scanit.html. [Accessed 09 Nov 2020].

[11] I. Corp., "IBM SPS Statistics Released for Windows, Version 27.0," IBM Corp., Armonk, NY, 2020.

[12] JMP, "Version Pro 14," SAS Institute Inc., Cary, NC, 1989-2019.

[13] A. Tohidi and N. B. Kaye, "Aerodynamic characterization of rod-like debris with application to firebrand transport," *Journal of Wind Engineering & Industrial Aerodynamics,* vol. 168, pp. 297-311, 2017.

[14] V. Chai, D. Parkhi, S. Boopathy, J. Xiang and J. Schlüter, "A model for the aerodynamic coefficients of rock-like debris," *Comptes Rendus Mecanique,* vol. 347, no. 1, pp. 19-32, 2019.

[15] A. Gilat and V. Subramaniam, Numerical Methods for Engineers and Scientists: An Introduction with Applications Using MATLAB, New Jersey: John Wiley & Sons, Inc., 2008.